


FULL PAPER

Open Access



Ionospheric responses on the 21 August 2017 solar eclipse by using three-dimensional GNSS tomography

C. H. Chen^{1*} , Charles C. H. Lin¹, C. J. Lee¹, J. Y. Liu^{2,3,4} and A. Saito⁵

Abstract

In this study, we have investigated the ionospheric responses on the August 2017 solar eclipse event by using a three-dimensional tomography algorithm with the ground-based GNSS (Global Navigation Satellite System) total electron content observations around Northern America. This three-dimensional ionospheric electron density structure from the tomography can provide us more information regarding the density variations and propagations of disturbances. Results show that the ionospheric electron density depletion triggered by the solar eclipse started from the higher ionosphere and then extended to lower altitudes. The maximum electron density depletion is around 40% compared with the previous day of solar eclipse. After around 30 min of the totality, the electron density continuously returned to the normal level. We further conduct a procedure of Fourier analyses to derive the vertical phase and group velocities of the electron density propagations. Results show that the opposite directions of the vertical phase and group velocities around 220–240 km altitude imply the energy/oscillation source by the solar eclipse.

Keywords: GNSS tomography, Solar eclipse, Wave propagation

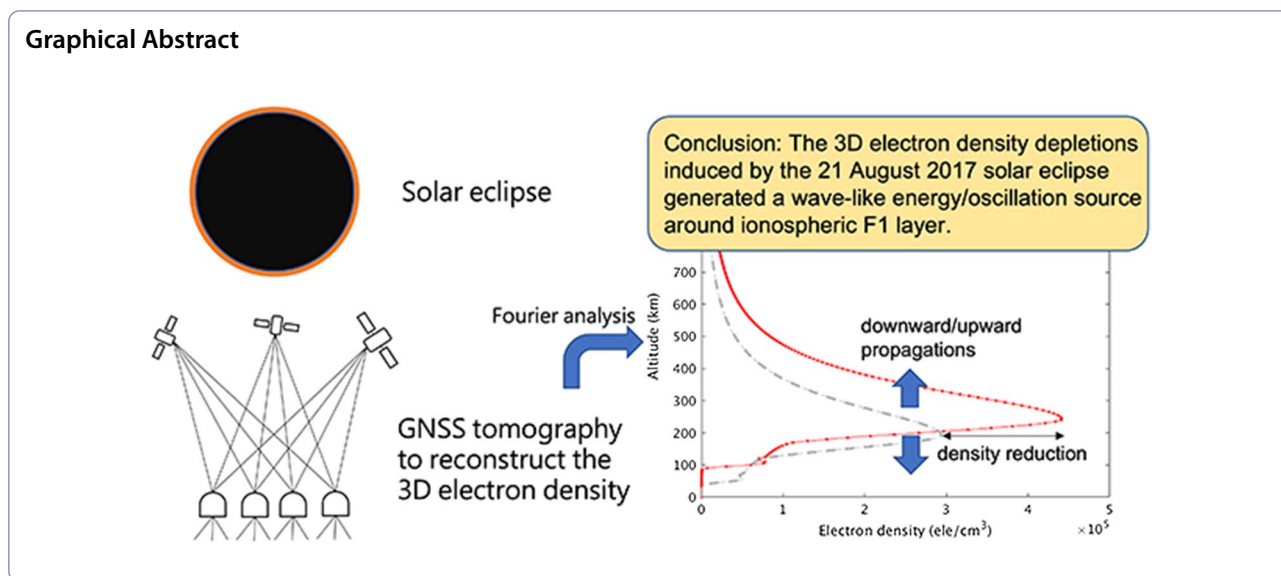
*Correspondence: koichi@mail.ncku.edu.tw

¹ Department of Earth Sciences, National Cheng Kung University, Tainan, Taiwan

Full list of author information is available at the end of the article



© The Author(s) 2022. **Open Access** This article is licensed under a Creative Commons Attribution 4.0 International License, which permits use, sharing, adaptation, distribution and reproduction in any medium or format, as long as you give appropriate credit to the original author(s) and the source, provide a link to the Creative Commons licence, and indicate if changes were made. The images or other third party material in this article are included in the article's Creative Commons licence, unless indicated otherwise in a credit line to the material. If material is not included in the article's Creative Commons licence and your intended use is not permitted by statutory regulation or exceeds the permitted use, you will need to obtain permission directly from the copyright holder. To view a copy of this licence, visit <http://creativecommons.org/licenses/by/4.0/>.



Introduction

A solar eclipse is the feature that the Moon's shadow projects on the Earth, leading a short shelter from the Sun. This provides us a good opportunity to investigate the ionospheric response to the solar eclipse. The solar eclipse-induced ionospheric electron density anomalies have been observed and discussed by many previous studies (e.g., Liu et al. 1998; Farges et al. 2001; Goncharenko et al. 2018). These anomalies are roughly divided to two periods, the eclipse and the post-eclipse. At the start of solar eclipse, the plasma density in the ionospheric *E* and *F1* regions will gradually decrease due to the loss of solar ionization rate. At the same time, the upward plasma diffusion at the ionospheric *F2* region becomes weaker. The plasma in the plasmasphere will downward supply the ionosphere by the gravity effect, which is similar to the nighttime ionosphere. This plasma downward diffusion from the plasmasphere will moderate the plasma reduction on the ionospheric *F2* region during the solar eclipse period (Le et al. 2009). After the moon shadow passes by, the ionospheric plasma will be increased due to the restoration of solar ionization rate. The plasma density after the solar eclipse was even higher than the normal ionospheric day, observed by previous studies (Huang et al. 1999; Jakowski et al. 2008; Cherniak and Zakharenkova, 2018). Furthermore, this enhancement of plasma density will continue few hours after the solar eclipse (Cherniak and Zakharenkova, 2018).

The ionospheric plasma density variations triggered by the total solar eclipse event on 21 August 2017 over the central United States have been investigated by many studies using the ground-based global positioning system (GPS) total electron content (TEC) observations,

showing the TEC depletion, the large-scale traveling ionospheric disturbances (LSTIDs), the wave-like electron density structures, and the TEC enhancement after the eclipse (Coster et al. 2017; Nayak and Yiğit 2018; Zhang et al. 2017; Cherniak and Zakharenkova, 2018; Goncharenko et al. 2018; Sun et al. 2018). However, the TEC is the integrated observation of ionospheric electron density along the ray path from a GPS satellite to a ground-based GPS receiver. It is hard to study the eclipse-induced electron density structure variation, especially in the vertical direction, by directly using the TEC observations. In this paper, a GPS tomography method (Seemala et al. 2014; Chen et al. 2016; Saito et al. 2017) is used to investigate the three-dimensional ionospheric electron density variations during the 2017 August solar eclipse event. Furthermore, a procedure of Fourier analysis (Kuo et al. 1993; Liu et al. 1998; 2007) is conducted to derive power spectra, vertical phase, and group velocities of the eclipse-triggered electron density variations.

GNSS ionospheric tomography

Around the mid-1980s, Austen et al. (1986, 1988) first suggested and applied the tomographic methodology to reconstruct the two-dimensional structure of the ionospheric electron density by using the line-of-sight TEC observations from Naval Navigational Satellite System (NNSS). The accuracy of ionospheric tomography is limited by the background ionospheric model, the incomplete ray geometry, and the measurement error, resulting in an ill-posed inverse problem. Many ionospheric tomography methods were published trying to reconstruct the ionospheric electron density structures (e.g., Austen et al. 1988; Raymund et al. 1994; Pryse 2003).

Recently, a new GPS ionospheric tomography algorithm has been developed by employing the dense ground-based GPS networks as well as the multiple Global Navigation Satellite System (GNSS) for solving this ill-posed inverse problem and further to reconstruct the three-dimensional structure of ionospheric electron density. In order to reduce the effect of background ionospheric or plasmaspheric electron density models as the initial condition on the reconstruction accuracy, a constrained least-square method is used in this GPS ionospheric tomography without using any initial model guess (Seemala et al. 2014). Later, Chen et al. (2016) applied this constrained GPS tomography method and successfully reconstructed the ionospheric electron density perturbation at the scale size of ~ 200 km in wavelength around Japan region, the medium-scale traveling ionospheric disturbance (MSTID), showing the capability of this GPS tomography for the investigation of disturbed ionosphere. Using the TEC observations provided by Japan GPS Earth Observation Network (GEONET), a near real-time ionospheric tomography system has been developed to continuously monitors the three-dimensional electron density variations over Japan every 15 min (Saito et al. 2017).

Similar to the Japan GEONET, there are ~ 2000 ground-based GNSS receivers located at North America (shown in Fig. 1), which provide lots of ionospheric TEC observations and are suitable to employ the GPS tomography for reconstructing the three-dimensional electron density structure. In this study, we applied the GPS tomography

algorithm by the method of Saito et al. (2017) over the North America region during the total solar eclipse period on 21 August 2017. Furthermore, not only the GPS signals, but also the GLOBAL Navigation Satellite System (GLONASS) signals are used to calculate the ionospheric TEC values along the ray paths from the satellites to the ground receivers for the first time. The increase of line-of-sight TEC observations can further reduce the effect of incomplete observational geometry on the electron density reconstruction accuracy. An elevation mask angle of 30° is set for the GNSS TEC observations used in this study.

The three-dimensional space of tomography is from - 125°E to - 71°E in longitude, 24°N to 52°N in latitude, and 80 km to 20,000 km in altitude. The resolutions are defined differently for trying to balance the observational path number in each grid and shown as follows. The longitudinal resolutions are set to 3° within - 112°E to - 91°E range and 2° outside (shown in Fig. 1). The latitudinal resolutions are set to 1° within 30°N to 44°N range and 2° outside (shown in Fig. 1). The vertical resolutions are 20 km within 80 km to 600 km range, 50 km within 650 km to 900 km range, 100 km within 1000 km to 2000 km range, and 5000 km within 5000 to 20,000 km range, respectively. Therefore, the total number of grids is 25,344 in the tomography space. A constraint term is applied in the cost function as shown as:

$$J(x) = \|b - Ax\|^2 + \lambda \|Wx\|^2, \tag{1}$$

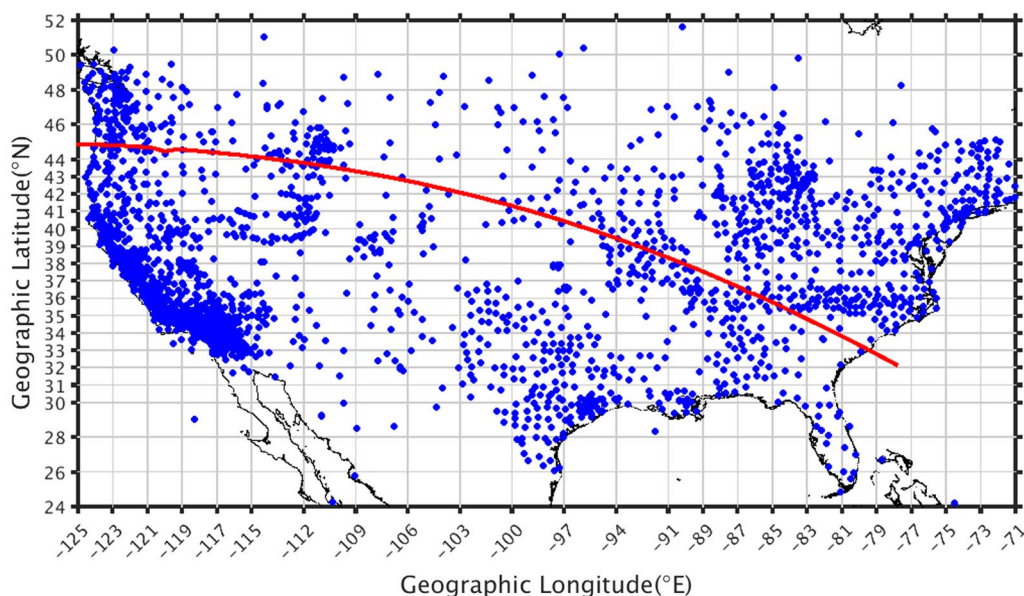


Fig. 1 The location of ~ 2000 ground-based GNSS receivers at Northern America. The blue dot is the GNSS receiver, and the red line indicates the path of total eclipse

where $J(x)$ is the cost function, showing the combination of least-square fitting (first term) and the constraint condition (second term) at the right-hand side. The parameters of x , and A indicate the matrixes of the electron concentration and the length of path in each grid, respectively. b matrix is the observed TEC values along the ray paths from the satellites to the ground GNSS receivers. The parameter, λ , is determined empirically to balance the least-square term and the constraint condition (Saito et al. 2017). W is the constraint matrix, which is a zero matrix but with the value of -1 at the six neighbor grids of x_{ij} (north, south, east, west, up, and down sides) and 6 at the center grid of x_i (see the appendix in Chen et al., 2016). Therefore, the definition of constraint condition in the cost function is the total electron density differences of each grid from its six neighbor grids, showing as:

$$Wx = \sum_{i=1}^N \sum_{j=1}^6 C_{ij} (x_i - x_{ij}) \tag{2}$$

where N is the total number grids, 25,344 in this case. C is the constraint parameter, which is determined as a function of latitude, longitude and altitude based on the empirical electron density model, NeQuick (DiGiovanni and Radicella, 1990; Radicella and Zhang, 1995). It is the weighting of constraint conditions in different altitudes (Seemala et al. 2014; Saito et al. 2017). A relatively small constraint parameter is applied around the high electron density regions, such as ionospheric F region and low-latitude regions, to allow the spacial variety in the electron density. Therefore, the electron density in each grid x , in Eq. (1) can be solved as,

$$x = (A^T A + \lambda W^T W)^{-1} A^T b. \tag{3}$$

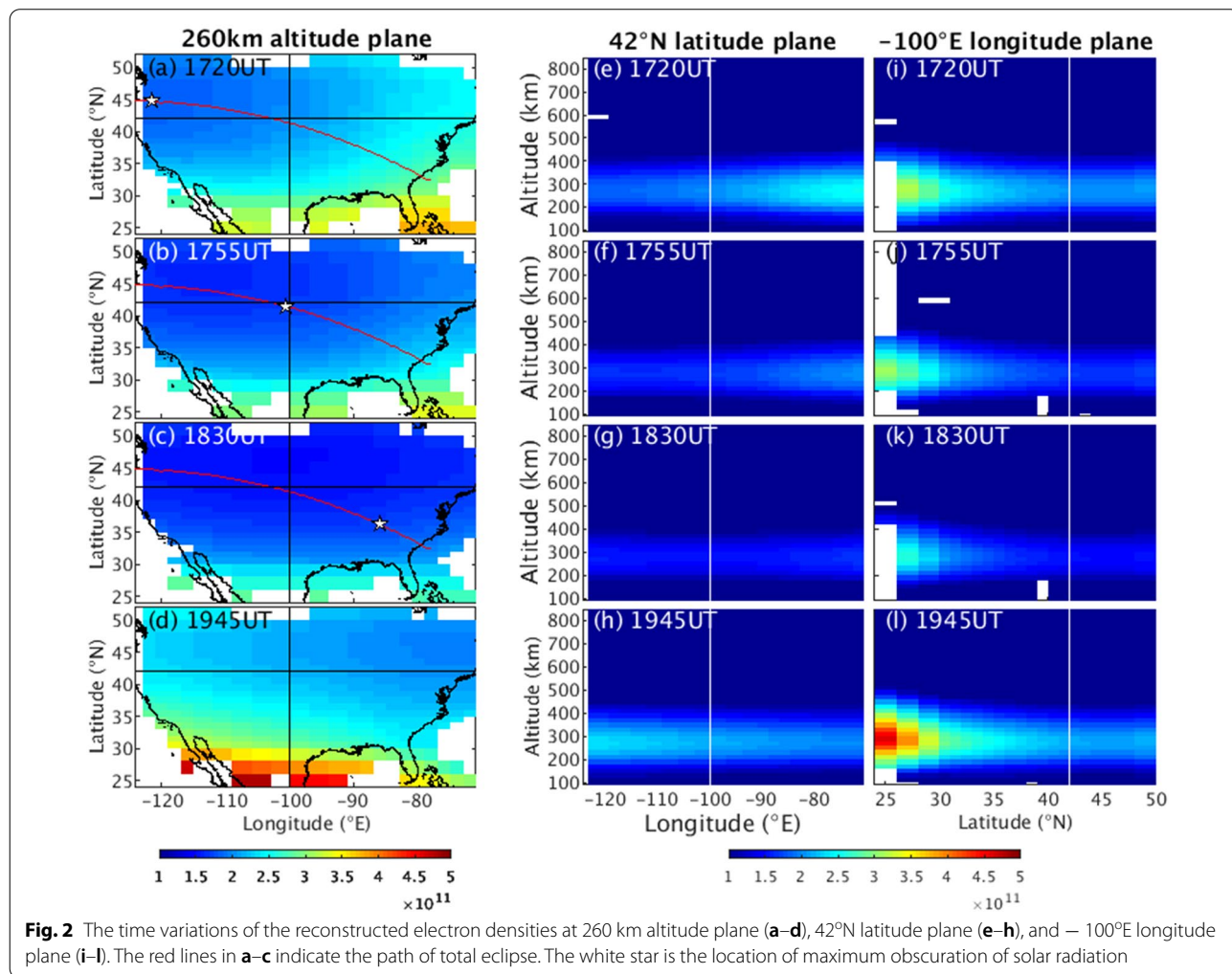


Fig. 2 The time variations of the reconstructed electron densities at 260 km altitude plane (a–d), 42°N latitude plane (e–h), and – 100°E longitude plane (i–l). The red lines in a–c indicate the path of total eclipse. The white star is the location of maximum obscuration of solar radiation

Tomography results

Figure 2 shows the time variations of the reconstructed electron densities by the 3D GNSS ionospheric tomography method at 260 km altitude plane (a–d), 42°N latitude plane (e–h), and – 100°E longitude plane (i–l), respectively. At 1720 UT, the ionospheric electron density depletion started from the north-west of American where is around the location of the solar eclipse maximum obscuration point (Fig. 2a). From the altitude–longitude plane along the latitude of 42°N (Fig. 2e), it also shows the lower electron densities appeared at the western American than the eastern. Then, the maximum obscuration point moved to the location around the latitude of 42°N and the longitude of – 100°E at 1755 UT (Fig. 2b). The maximum electron density depletion appeared at the north-west of obscuration region (around the longitude of – 110°E and the latitude of 46°N), which also can be seen in the fixed altitude and latitude planes (Fig. 2b, f). Besides, the start time of eclipse at the location of (42°N, – 70°E) was ~ 1730 UT. It shows that the electron density depletion (as compared to Fig. 2e) in Fig. 2f at the east edge, – 70°E longitude, was affected by the decrease of solar radiation. At 1830 UT, the maximum electron density depletion moved to the longitude of – 100°E, following the movement of solar eclipse maximum obscuration (Fig. 2c). After the solar eclipse, 1945 UT, the solar ionization rate returned to the normal level and triggered the increases of ionospheric electron density at all the American region (Fig. 2d). These electron density reductions and increases are also shown in the fixed latitude

(Fig. 2e–h) and longitude (Fig. 2i–l) planes during and after the solar eclipse.

In order to investigate the ionospheric response to the total solar eclipse and compare with previous studies (Nayak and Yiğit 2018; Uma et al. 2020), the electron density variation is calculated by subtracting the reconstructed electron densities on the previous day (20 August 2017), called as reference day afterwards, from those on the eclipse day (21 August 2017). Furthermore, the difference percentage of electron density is defined as

$$\frac{Ne_d - Ne_{d-1}}{Ne_{d-1}} \times 100, \tag{4}$$

where Ne is the electron density. The index words in Eq. (4), d and $d-1$, indicate the eclipse day and the reference day, respectively. Figure 3 shows the electron density variations as well as the difference percentage at 1755 UT at 260 km altitude plane (a–b), 42°N latitudinal plane (c–d), and – 100°E longitudinal plane (e–f). Figure 3a clearly shows that the electron density depletions appeared around the lower latitude regions compared with the reference day. The electron densities variations at the 42°N latitudinal plane (Fig. 3c) and the – 100°E longitude plane (Fig. 3e) further show the most density depletion appeared at the west and south of maximum obscuration, respectively, and mainly around the altitude of 260 km. The difference percentage of electron density (Fig. 3d, f) shows that the more electron density depletion appeared at the lower altitude regions on the west side of – 100°E longitude. The most electron density

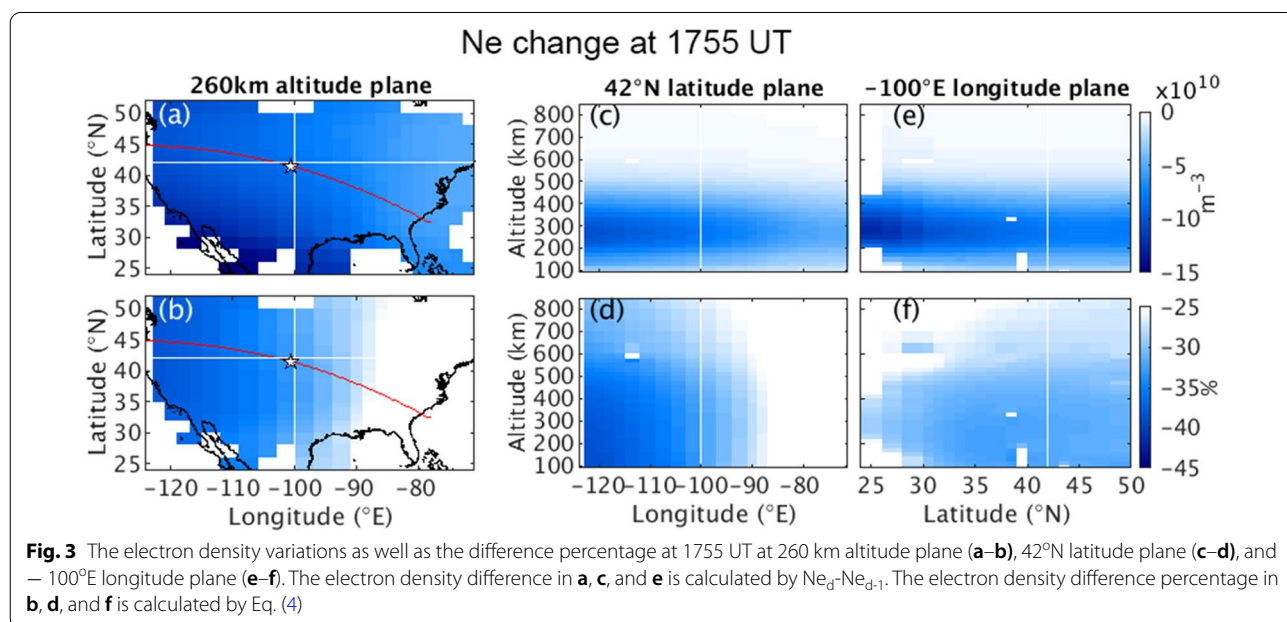
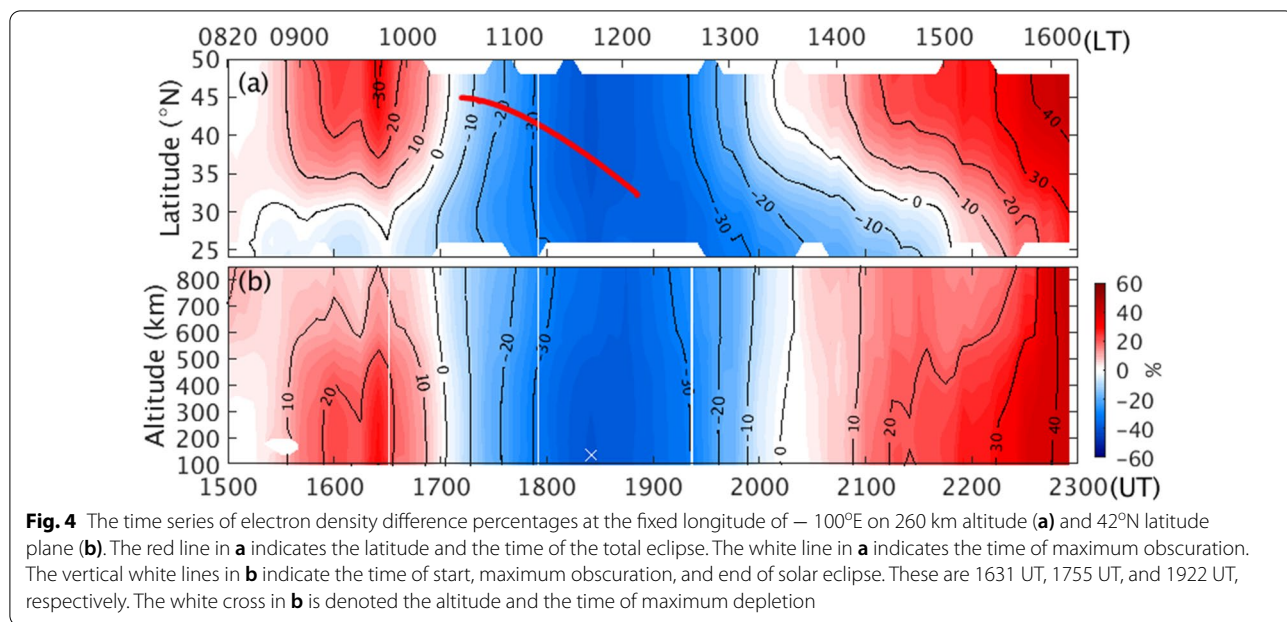


Fig. 3 The electron density variations as well as the difference percentage at 1755 UT at 260 km altitude plane (a–b), 42°N latitude plane (c–d), and – 100°E longitude plane (e–f). The electron density difference in a, c, and e is calculated by $Ne_d - Ne_{d-1}$. The electron density difference percentage in b, d, and f is calculated by Eq. (4)



depletion is around 40% compared with the reference day.

The time series of electron density difference percentages at the fixed longitude of -100°E on 260 km altitude (Fig. 4a) and 42°N latitude planes (Fig. 4b) are presented, respectively. Compared with the electron density on and before the eclipse day, the electron density depletion, denoted by the contour curve of 0%, started from the lower latitude shown in Fig. 4a region around 1700 UT. In addition, the electron density depletion of 0% contour curve in Fig. 4b first appeared at the higher altitude and then extended to the lower altitude after the start time of eclipse, around 1631 UT. After 1730 UT, the contour curves of -20% and -30% in Fig. 4b show that the

electron density reduction is upward propagation until 1845 UT. The results further show that the electron density depletion was mainly concentrated on the altitudes lower than 600 km and reached its maximum depletion at 140 km altitude at 1825 UT, about 30 min after the time of eclipse maximum obscuration (1755 UT, denoted by the vertical white line). The maximum depletion was around -39.9% . After 1845 UT, the electron density continuously returned to the normal level until 2030 UT. Due to the southward move of solar eclipse obscuration shown by the red curve in Fig. 4a, the electron density at lower latitude region returned to its normal level until 2100 UT.

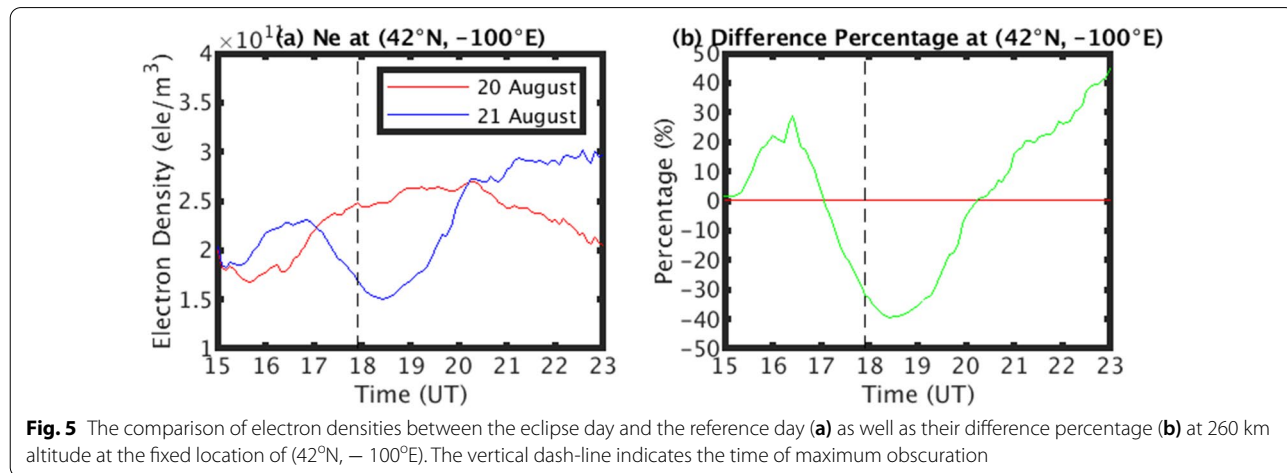


Figure 5 shows the comparison of electron densities between the eclipse day and the reference day (a) as well as their difference percentage (b) at 260 km altitude at the fixed location of (42°N, − 100°E). Results show that the maximum electron density depletion on the eclipse day appeared around 15–30 min after the totality (vertical-black-dashed line in Fig. 5a) and reached around 40% compared with the reference day (Fig. 5b). The depletion rate of electron density at 260 km is around 5.33×10^{10} ele/m³/hr ($= (2.3 \times 10^{11} - 1.5 \times 10^{11}) / 1.5$ h). Later, the electron density returned to the reference day level around 2010 UT (~1330 LT) with an increasing rate of 7.19×10^{10} ele/m³/h ($= (2.7 \times 10^{11} - 1.5 \times 10^{11}) / 1.67$ h), and then kept its concentration for a few hours (Fig. 5a). These time delay and the electron density recovery features are clearly shown in the difference percentage (Fig. 5b). Noted that the increase of difference percentage after 2010 UT in Fig. 5b is due to the coupled effects of the decrease of electron density on the reference day and the preservation of electron density on the eclipse day. After 2010 UT (~1320 LT), because of the descending solar zenith angle, the photochemical ionization rate becomes weak and then results in the electron density decrease on the reference day. However, after the maximum obscuration on the eclipse day, the electron density can be preserved a long time by the effects of downward plasma fluxes from the topside ionosphere, like the downward plasma diffusion after sunset, and the production of plasma by the recovery of ionization in the bottom side ionosphere (Cherniak and Zakharenkova, 2018).

Discussion

Due to the solar radiation disruption by the eclipse, the photochemical, transport, and thermal processes of the ionosphere will be changed and lead to the reduction of electron density. The TEC derived from the highly dense GNSS networks over North America provides a good opportunity to investigate the spacial and temporal variations of the ionospheric responses to the total solar eclipse event on 21 August 2017. Previous results show that the maximum TEC depletion during this eclipse period was around 50–60% compared with the background level (Coster et al. 2017; Cherniak and Zakharenkova, 2018) and the TEC enhancement was up to 20–30% after the eclipse (Cherniak and Zakharenkova, 2018). The reconstruction of 3D electron density by the GNSS tomography in this study further shows the maximum depletion of electron density, compared with the reference day, mainly occurred around the 300 km altitude (Fig. 3c, e) and distributed to the higher altitudes with the maximum depletion of 40% (Figs. 3d, f, 5b). This result is consistent with other ionospheric observations, such as the electron density from the Millstone Hill incoherent

scatter radar (Goncharenko et al. 2018) and the electron density profile from the COSMIC RO (Uma et al. 2020), for the same solar eclipse event.

Compared with the reference day, Fig. 4b further shows that the electron density depletions with the level of − 20% and − 30% after 1730 UT primarily started from the lower ionosphere and then extended to the higher ionosphere. This is because the electron concentrations in the ionospheric E and F1 region are mainly controlled by the solar radiation through the photochemical processes (Müller-Wodarg et al. 1998). During the solar eclipse period, the solar radiation is masked by the moon shadow, the responses of electron density at the lower part of ionosphere are relatively immediate, whereas the higher part of ionosphere is later. Furthermore, after the eclipse around 1900 UT, the electron density recovery also started from the lower altitude region (Fig. 4b) and then extended to the higher altitude region, which caused by the restoration of solar ionization rate.

Since the GNSS tomography can provide us the 3D structure of electron density, we further adopt the procedure of Fourier analyses (Kuo et al. 1993; Liu et al. 1998; 2007) deriving the vertical phase and group velocities of ionospheric responses to the solar eclipse. The time series of the electron density on the eclipse day, $P(z, t)$, at the fixed location of (42°N, − 100°E) can be expressed as

$$P(z, t) = A_0 + \sum_{j=1}^{N/2} (A_j \cos \omega_j t + B_j \sin \omega_j t) \quad (5)$$

where N is the number of data points. ω_j is the angular frequency of the j th harmonic ($= \frac{2\pi \bullet j}{N \Delta t}$), where Δt is the data sampling rate, which is 300 s (or 5 min) in this study. Therefore, the amplitude, $C_j(z)$, and the phase, $\Phi_j(z)$, at a certain altitude z are defined as $\sqrt{A_j^2 + B_j^2}$ and $\tan^{-1}(\frac{B_j}{A_j})$, respectively. The vertical wave number k_j can be obtained by the differentiating $\Phi_j(z)$ with respect to z , $\frac{d\Phi_j(z)}{dz}$. Consequently, the vertical phase velocity is given as

$$v_p = \frac{\omega_j}{k_j}. \quad (6)$$

Furthermore, the vertical group velocity of a wave packet centered at the center frequency can be given as

$$v_g = \frac{d\omega}{dk}. \quad (7)$$

By successively changing the data length from $T = N \Delta t$ to $T' = (N - \Delta N) \Delta t$, where ΔN is the change of data points. In this study, ΔN is set to be 2 and Δt is 300 s (5 min.). The analysis period is from 1700 to 2255 UT, indicating the N is 72. The small difference of angular

frequency $d\omega$, near the center frequency of the wave packet is defined as

$$d\omega = \omega'_j - \omega_j = \frac{2\pi \cdot j}{(N - \Delta N)\Delta t} - \frac{2\pi \cdot j}{N\Delta t}. \quad (8)$$

The change of vertical wave number dk , is

$$dk = k'_j - k_j = \frac{d\Phi'_j(z)}{dz} - \frac{d\Phi_j(z)}{dz}. \quad (9)$$

Figure 6 shows the normalized power spectra of temporal variations in the electron density on the eclipse day at various altitudes. It is clearly seen that the center frequency (period) of relatively larger powers change with altitudes. Results show the period of 72.5 min. (~ 0.2299 mHz) during 100–300 km altitude, 75.0 min. (~ 0.2222 mHz) during 320–400 km altitude, 77.5 min. (~ 0.2151 mHz) during 420–460 km altitude, 72.5 min. (~ 0.2299 mHz) at 480 km altitude, 67.5 min. (~ 0.2469 mHz) during 500–540 km altitude, 65.0 min. (~ 0.2564 mHz) at 560 km altitude, and 62.5 min. (~ 0.2667 mHz) higher than 580 km altitude. These periods are similar to the previous results for the same solar eclipse event by Nayak and Yiğit (2018), which reported the gravity wave-like signature of GPS TEC with spread wave periods around 20–90 min. during the eclipse by using the Hilbert–Huang Transformation (HHT) technique (Huang et al. 1998). This study further shows that the primary waves of electron density depletion caused by the solar eclipse generally has the longer periods toward the higher altitudes around 460 km and then become shorter above.

To further see the wave structure of electron density, the summation of Fourier analyzed amplitudes between 67.5 and 77.5 (72.5 \pm 5) min (like a bandpass filter) at different altitude is calculated. Result in Fig. 7 shows a clear wavy structure of electron density fluctuation between 100 and 450 km altitude. At the beginning of the solar eclipse ~ 1700 UT, the downward phase propagation of ionospheric disturbance appears, and then gradually turns to the upward phase propagation after 2000 UT. It reveals the vertical phase change of the electron density disturbance during the solar eclipse period.

Following Eqs. (6), (7), we then calculate the phase and group velocities of each pronounced wave with its center frequency (period) at the certain altitude. Figure 8 summarizes the phase and group velocities at various altitudes, revealing the vertical phase velocities of 80–170 m/s upward below the altitude of 180 km, 30–130 m/s downward between the altitude of 200 and 300 km, 10–240 m/s upward between 340 and 440 km, 20–70 m/s downward between 460 and 560 km, and 100–130 m/s above the altitude of 600 km, respectively.

Moreover, the vertical group velocities below 240 km altitude are in the downward direction with the velocity range of 10–50 m/s. Between the altitude of 260–320 km, the group velocities are in the upward direction with the velocity range of 5–50 m/s.

According to the linear gravity wave theory (Holton and Hakim, 2013), one of the important properties of gravity waves is the opposite directions of the group and phase velocities in the vertical direction. Here, the upward (downward) phase velocity lower (higher) than 200 (260) km altitude, together with the downward (upward) group velocity, suggest the characteristics of the gravity wave that propagates downward (upward). The change direction of gravity wave propagation around 220–240 km altitude shown in Fig. 8 indicates the possible energy/oscillation source of the pronounced waves. The mechanism responsible to generation of gravity wave might be the atmospheric cooling/heating during eclipse period (Liu et al. 1998), which leads to the change of scale height. The scale height is a parameter commonly used to describe the vertical variation of the atmosphere. It is defined as the height when the atmospheric density is reduced by a factor of $1/e$. Therefore, the small value of scale height means that the atmosphere is more concentrated near the surface. At the beginning of eclipse, the thermal cooling of plasma and neutral gases lead to the reductions of scale height and then result in the overall downward diffusion of atmosphere. Since the ionospheric electron density is produced by the ionization processes of neutral gases, the decreased height of neutral gases as well as the decrease of solar radiation will cause the altitude reduction of electron density production. After the maximum obscuration, the atmospheric scale height and the electron density are increased by the recovery of solar radiation and then the electron density diffuses upward to the higher altitude. As a result, the fluctuating motions of the atmosphere around 220–240 km altitude act as an energy/oscillation source of gravity waves and the signature reflects to the plasma motion in the ionosphere as what was observed in this study. The feature was also reported by the previous eclipse studies (Altadill et al. 2001; Liu et al. 1998). During the 360–420 km altitudes, the group velocity has the same direction with the phase velocity, showing that the group velocity might be modified by the stronger background wind or the wind shear. This process may lead the wave packet no longer follows the linear gravity wave theory (Kuo et al. 1992; Huang et al. 1992).

Conclusion

The reconstructed three-dimensional electron densities over Northern America were employed to study the ionospheric responses on the August 2017 solar eclipse by

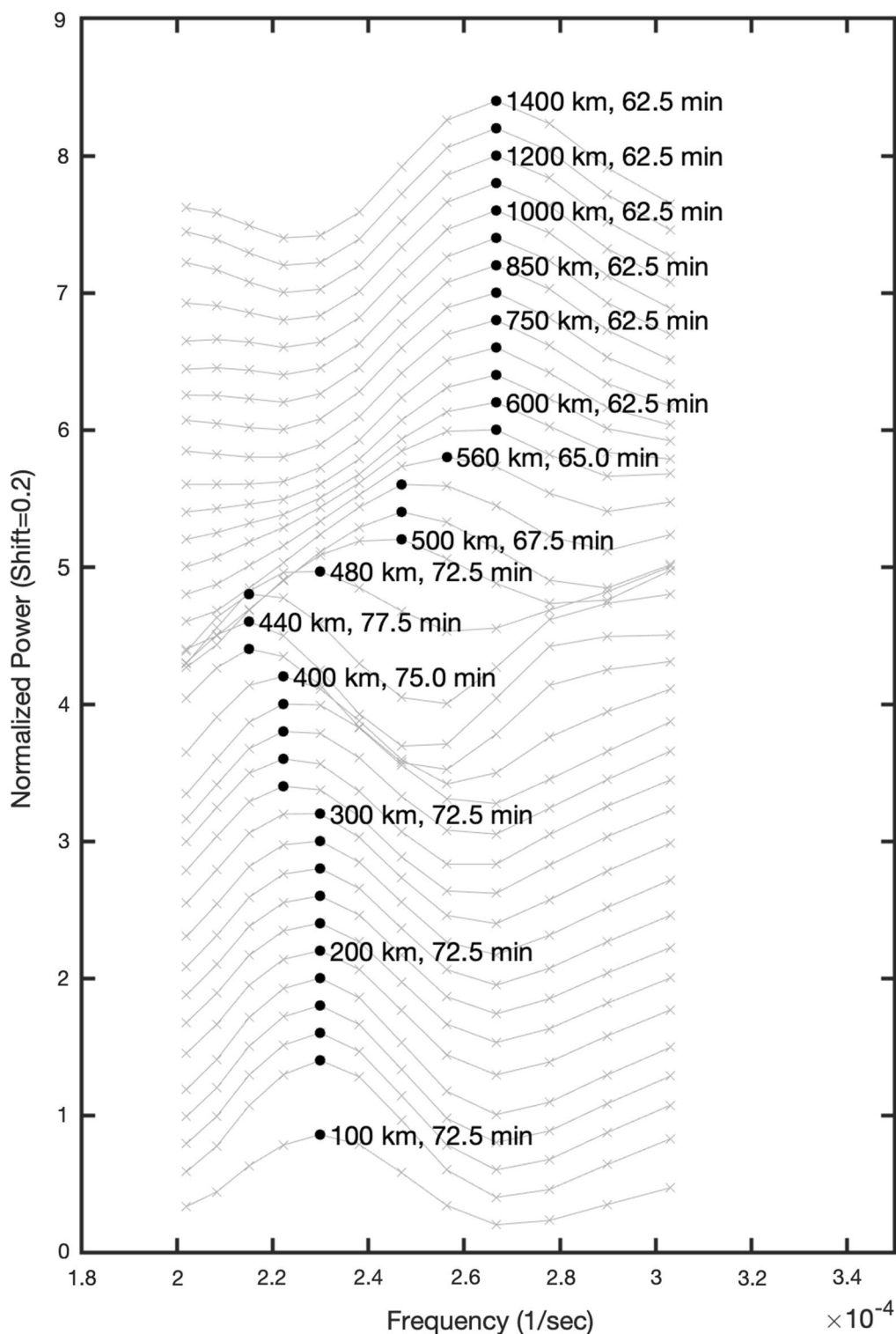
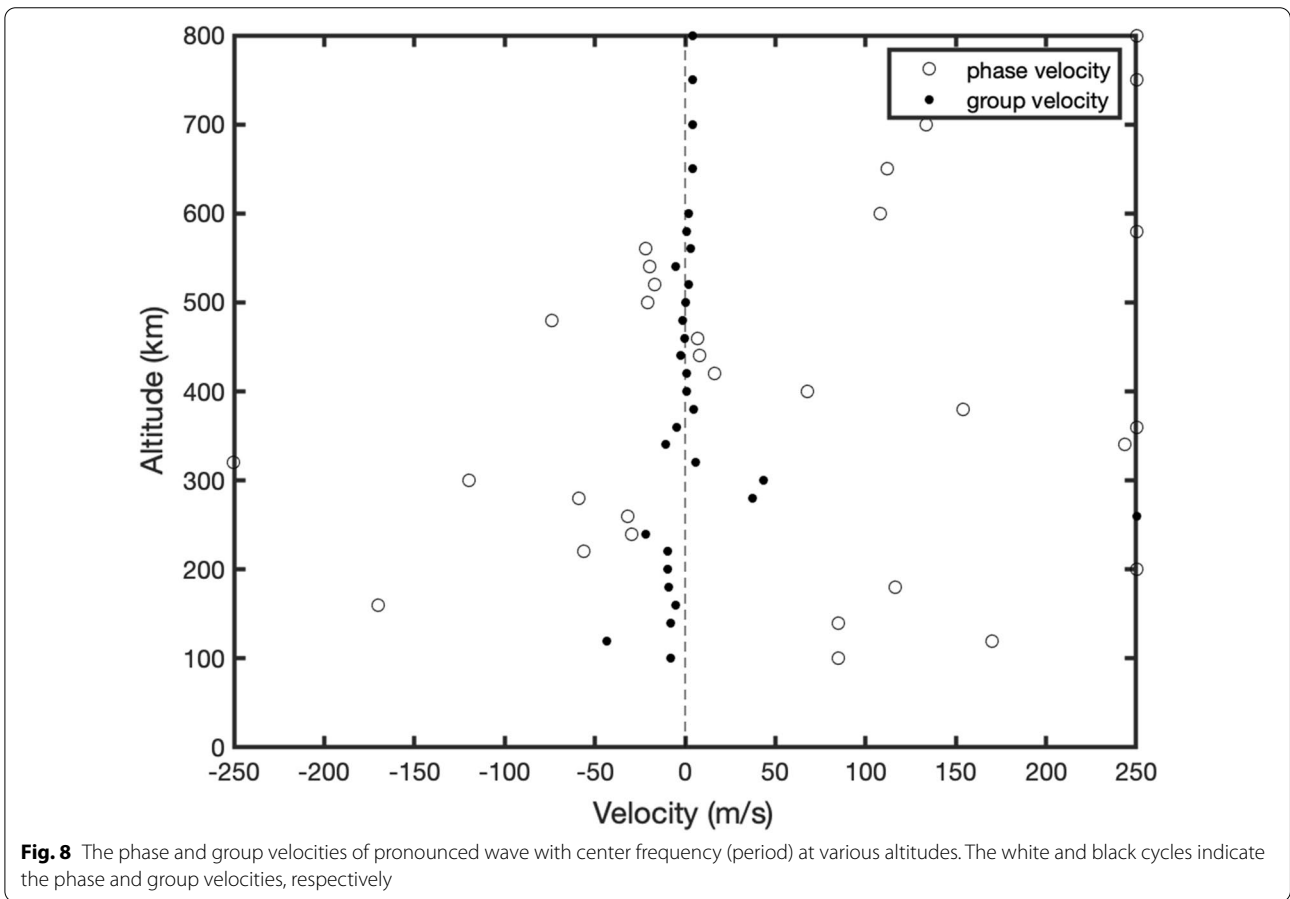
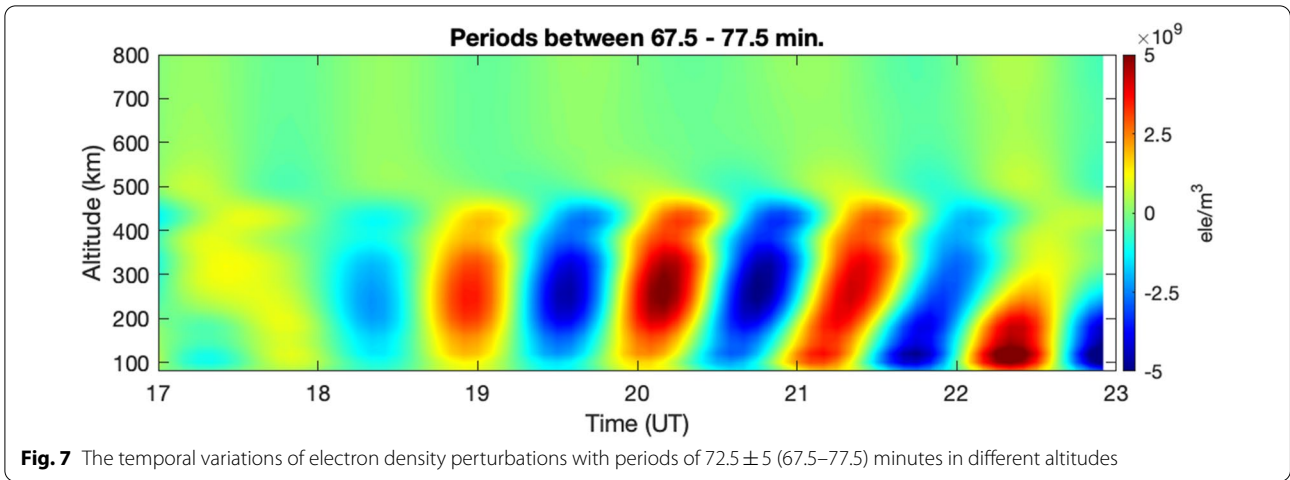


Fig. 6 The normalized power spectra of temporal variations in the electron density on the eclipse day at various altitudes. The black dot denotes the center frequency (period) of each pronounced wave. In order not to overlap the spectrum results at each altitude, the shift value of 0.2 is added in each altitude



the GNSS tomography method. We further derived the TEC observations from GLONASS satellites to reduce the effect of incomplete observational geometry and improve the accuracy of electron density reconstruction in this study. Compared with the two-dimensional TEC

observations, the three-dimensional electron density can provide us more information to further study the variations and propagations of eclipse-induced electron density in the vertical direction. The major findings are as follows:

1. The mainly depletion of electron density caused by the disruption of solar radiation occurred around 260 km altitude. The electron density difference percentages further show the depletion started from the higher ionosphere and then extended to the lower altitude.
2. The electron density decreased up to 40% compared with the reference day around 30 min after the maximum obscuration.
3. The pronounced waves of electron density perturbation with periodicities around 62.5–77.5 min were detected during the solar eclipse by the Fourier analyses. Furthermore, the pronounced waves generally have the longer periods toward the higher altitudes around 460 km and then become shorter periods above.
4. The change signs of the vertical group velocities imply the possible energy/oscillation source of the pronounced waves around 220–240 km altitude. Results further show that the energy propagates as a gravity wave following the linear gravity wave theory below 320 km altitudes.

In conclusion, the three-dimensional electron density structures by GNSS tomography method together with the vertical wave propagations by Fourier analysis provide a powerful tool to study the dynamic processes of electron density distributions in the ionosphere. The horizontal wave propagation of electron density perturbations will be further analyzed and discussed in future works.

Acknowledgements

We thank Prof. M. Yamamoto and Dr. S. Saito for the helpful improvement on the GNSS tomography procedure and Dr. C.C. Hsiao for the discussions of Fourier analysis on the wave propagation.

Author contributions

CHC has carried out the calculations of GNSS TEC, analyzed the wave propagation, and drafted the manuscript. CJL has run the GNSS tomography and program coding. CHL, JYL and AS have critically provided scientific contents and discussions. All authors read and approved the final manuscript.

Funding

This paper is supported by Ministry of Science and Technology (MOST) of Taiwan to National Cheng Kung University under MOST-110-2111-M-006-002, MOST-110-2121-M-006-010 and MOST-111-2111-M-006-003.

Availability of data and materials

The TEC data from ground-based GNSS receivers are available at CDDIS (https://cddis.nasa.gov/Data_and_Derived_Products/GNSS/daily_30second_data.html). The start and end time of solar eclipse is calculated by the Local Circumstances Calculator (http://xjubier.free.fr/en/site_pages/SolarEclipseCalc_Diagram.html).

Declarations

Competing interests

The authors declare that they have no competing interests.

Author details

¹Department of Earth Sciences, National Cheng Kung University, Tainan, Taiwan. ²Center for Astronautical Physics and Engineering, National Central University, Taoyuan, Taiwan. ³Department of Space Science and Engineering, National Central University, Taoyuan, Taiwan. ⁴Center for Space and Remote Sensing Research, National Central University, Taoyuan, Taiwan. ⁵Department of Geophysics, Kyoto University, Kyoto, Japan.

Received: 1 April 2022 Accepted: 5 November 2022

Published online: 26 November 2022

References

- Altadill D, Sole JG, Apostolov EM (2001) Vertical structure of a gravity wave like oscillation in the ionosphere generated by the solar eclipse of August 11, 1999. *J Geophys Res* 106(A10):21419–21428
- Austen JR, Franke SJ, Liu CH (1988) Ionospheric imaging using computerized tomography. *Radio Sci* 23(3):299–307
- Austen, J. R., Franke, S. J., Liu, C. H., and Yeh, K. C. (1986), Applications of computerized tomography techniques to ionospheric research, In: International Beacon Satellite Symposium June 9–14, Oulu Finland, Proceeding part 1 25–36.
- Chen CH, Saito A, Lin CH, Yamamoto M, Suzuki S, Seemala GK (2016) Medium-scale traveling ionospheric disturbances by three-dimensional ionospheric GPS tomography. *Earth Planets Space* 68:32
- Cherniak I, Zakharenkova I (2018) Ionospheric total electron content response to the great American solar eclipse of 21 August 2017. *Geophys Res Lett*. <https://doi.org/10.1002/2017GL075989>
- Coster AJ, Goncharenko L, Zhang S-R, Erickson PJ, Rideout W, Vierinen J (2017) GNSS observations of ionospheric variations during the 21 August 2017 solar eclipse. *Geophys Res Lett*. <https://doi.org/10.1002/2017GL075774>
- DiGiovanni G, Radicella SR (1990) An analytical model of the electron density profile in the ionosphere. *Adv Space Res* 10:27–30
- Farges T, Jodogne JC, Bamford R, Le Roux Y, Gauthier F, Vila PM, Altadill D, Sole JG, Miro G (2001) Disturbances of the western European ionosphere during the total solar eclipse of 11 August 1999 measured by a wide ionosonde and radar network. *J Atmos Solar—Terr Phys* 63(9):915–924
- Goncharenko LP, Erickson PJ, Zhang S-R, Galkin I, Coster AJ, Jonah OF (2018) Ionospheric response to the solar eclipse of 21 August 2017 in Millstone Hill (42N) observations. *Geophys Res Lett* 45:4601–4609. <https://doi.org/10.1029/2018GL077334>
- Holton and Hakim (2013) *An Introduction to Dynamic Meteorology*, 5th edn. Academic Press, Cambridge
- Huang CM, Kuo FS, Lue HY, Liu CH (1992) Numerical simulations of the saturated gravity wave spectra in the atmosphere. *J Atmos Terr Phys* 54:129
- Huang NE, Shen Z, Long SR, Wu MC, Shih HH, Zheng Q, Liu HH (1998) The empirical mode decomposition and the Hilbert spectrum for nonlinear and non-stationary time series analysis. *R Soc London Proc* 454:903–998
- Huang CR, Liu CH, Yeh KC, Lin KH, Tsai WH, Yeh HC, Liu JY (1999) A study of tomographically reconstructed ionospheric images during a solar eclipse. *J Geophys Res* 104:79–94. <https://doi.org/10.1029/98JA02531>
- Jakowski N, Stankov M, Wilken V, Borries C, Altadill D, Chum J et al (2008) Ionospheric behavior over Europe during the solar eclipse of 3 October 2005. *J Atmos Solar Terr Phys* 70(6):836–853
- Kuo FS, Lue HY, Huang CM, Lo CL, Liu CH, Fukao S, Muraoka Y (1992) A study of velocity fluctuation spectra in the troposphere and lower stratosphere using MU-radar. *J Atmos Terr Phys* 54:34
- Kuo FS, Lee KE, Lue HY, Liu CH (1993) Measurement of vertical phase and group velocities of atmospheric gravity waves by VHF radar. *J Atmos Terr Phys* 55(9):1193–1201
- Le H, Liu L, Yue X, Wan W (2009) The ionospheric behavior in conjugate hemispheres during the 3 October 2005 solar eclipse. *Ann De Geophysique* 27:179–184. <https://doi.org/10.5194/angeo-27-179-2009>
- Liu JY, Hsiao CC, Tsai LC, Liu CH, Kuo FS, Lue HY, Huang CM (1998) Vertical phase and group velocities of internal gravity waves derived from ionograms during the solar eclipse of 24 October 1995. *J Atmos Solar Terr Phys* 60:1679–1686
- Liu JY, Hsiao CC, Liu CH, Yamamoto M, Fukao S, Lue HY, Kuo FS (2007) Vertical group and phase velocities of ionospheric waves derived from the MU radar. *Radio Sci* 40:RS4014. <https://doi.org/10.1029/2005RS003435>

- Müller-Wodarg ICF, Aylward AD, Lockwood M (1998) Effects of a mid-latitude solar eclipse on the thermosphere and ionosphere—a modelling study. *Geophys Res Lett* 25(20):3787–3790
- Nayak C, Yiğit E (2018) GPS-TEC observation of gravity waves generated in the ionosphere during 21 August 2017 total solar eclipse. *J Geophys Res Space Physics*. <https://doi.org/10.1002/2017JA024845>
- Pryse SE (2003) Radio tomography: a new experimental technique. *Surv Geophys* 24:1–38
- Radicella SM, Zhang ML (1995) The Improved DGR analytical model of electron density height profile and total electron content in the ionosphere. *Ann Geofis* 38:35–41
- Raymund TD, Franke SJ, Yeh KC (1994) Ionospheric tomography: its limitations and reconstruction methods. *J Atmos Phys* 56:637–657
- Saito S, Suzuki S, Yamamoto M, Saito A, Chen CH (2017) Real-time ionosphere monitoring by three-dimensional tomography over Japan. *J Inst Navig* 64:4
- Seemala GK, Yamamoto M, Saito A, Chen CH (2014) Three-dimensional GPS ionospheric tomography over Japan using constrained least squares. *J Geophys Res Space Phys* 119:3044–3052. <https://doi.org/10.1002/2013JA019582>
- Sun YY, Liu JY, Lin CH, Lin CY, Shen MH, Chen CH, Chou MY (2018) Ionospheric bow wave induced by the moon shadow ship over the continent of United States on 21 August 2017. *Geophys Res Lett*. <https://doi.org/10.1002/2017GL075926>
- Uma G, Brahmanandam PS, Srinivasu VKD, Prasad DSVD, Gowtam VS, Tulasi Ram S, Chu YH (2020) Ionospheric responses to the 21 August 2017 great American solar eclipse—a multi-instrument study. *Adv Space Res* 65(1):74–85
- Zhang S-R, Erickson PJ, Goncharenko LP, Coster AJ, Rideout W, Vierinen J (2017) Ionospheric bow waves and perturbations induced by the 21 August 2017 solar eclipse. *Geophys Res Lett*. <https://doi.org/10.1002/2017GL076054>

Publisher's Note

Springer Nature remains neutral with regard to jurisdictional claims in published maps and institutional affiliations.

Submit your manuscript to a SpringerOpen® journal and benefit from:

- Convenient online submission
- Rigorous peer review
- Open access: articles freely available online
- High visibility within the field
- Retaining the copyright to your article

Submit your next manuscript at ► [springeropen.com](https://www.springeropen.com)
